L1 ribozyme catalysis and regioselectivity. The ribose of U71 that contains the 3′-hydroxyl nucleophile of the ligation reaction participates in an extensive hydrogen-bonding network within the catalytic pocket including the A39 phosphate of stem C, and the 2′-hydroxyl of U38 via water W13 (Fig. 4C). This network suggests why the L1 ligase is regioselective for formation of the biologically relevant 5′ to 3′ phosphodiester bond rather than a 5′ to 2′ bond. The 3′-oxygen of U71 in the ligation product is only 2.9 Å from the nonbridging phosphate oxygen that is coordinated with the ligation-site Mg^{2+} ion. Although clearly within hydrogen-bonding distance, the 3′-oxygen cannot donate a hydrogen bond to the phosphate oxygen because it has already formed an ester linkage to the G1 phosphate. If the positions of these atoms are retained in the preligation complex, the O1P phosphate of A39 would be ideally positioned to abstract a proton from the 3′-oxygen, thus generating the attacking nucleophile. Although the 2′-hydroxyl of U71 also resides within potential hydrogen-bonding distance to this phosphate oxygen, it, unlike the 3′-oxygen, has a tightly bound water molecule as a hydrogen-bonding partner. This water molecule, W13, interacts specifically not only with the 2′-hydroxyl of U71, but also with the 2′-hydroxyl of U38, the exocyclic amine of G52, and possibly, the exocyclic oxygen of U71 (Fig. 4C). This hydrogen-bonding network may sequester the 2′-hydroxyl of U71 away from the ligation-site phosphate, and in the event of deprotonation, the 2′-alkoxide might be resupplied with a proton from water W13, which would effectively quench the side reaction (Fig. 4D).

The in vitro–evolved L1 RNA ligase ribozyme, therefore, appears to fold into a compact structure in which a set of invariant nucleotides interact to create a catalytic pocket capable of juxtaposing the ligation ends with a bound Mg^{2+} ion cofactor. The network of specific structural interactions that promote catalysis of phosphodiester bond formation, including transition-state stabilization interactions and functional group positioning for general base catalysis, as well as the propensity to fold into a preformed active site capable of binding a substrate and a metal ion cofactor, are each reminiscent of what has been observed in several natural ribozymes. The L1 ligase ribozyme thus demonstrates, in principle, that RNA indeed has the ability to evolve into a structure capable of catalyzing regiospecific phosphodiester bond ligation and appears to use strategies of transition-state stabilization and acid-base catalysis similar to those that exist for natural ribozymes and protein enzymes.

References and Notes

1. K. Kruger *et al.*, *Cell* **31**, 147 (1982).
2. C. Guerrier-Takada, K. Gardiner, T. Marsh, N. Pace, S. Altman, *Cell* **35**, 849 (1983).
3. A. J. Zaug, T. R. Cech, *Science* **231**, 470 (1986).
4. R. F. Gesteland, J. F. Atkins, Eds., *The RNA World* (Cold Spring Harbor Laboratory Press, Plainview, New York, 1993).
5. J. A. Doudna, T. R. Cech, *Nature* **418**, 222 (2002).
6. K. E. McGinness, G. F. Joyce, *Chem. Biol.* **10**, 5 (2003).
7. D. P. Bartel, J. W. Szostak, *Science* **261**, 1411 (1993).
8. E. H. Ekland, J. W. Szostak, D. P. Bartel, *Science* **269**, 364 (1995).
9. M. P. Robertson, A. D. Ellington, *Nat. Biotechnol.* **17**, 62 (1999).
10. L. F. Landweber, I. D. Pokrovskaya, *Proc. Natl. Acad. Sci. U.S.A.* **96**, 173 (1999).
11. J. Rogers, G. F. Joyce, *Nature* **402**, 323 (1999).
12. L. Jaeger, M. C. Wright, G. F. Joyce, *Proc. Natl. Acad. Sci. U.S.A.* **96**, 14712 (1999).
13. Y. Ikawa, K. Tsuda, S. Matsumura, T. Inoue, *Proc. Natl. Acad. Sci. U.S.A.* **101**, 13750 (2004).
14. W. K. Johnston, P. J. Unrau, M. S. Lawrence, M. E. Glasner, D. P. Bartel, *Science* **292**, 1319 (2001).
15. M. S. Lawrence, D. P. Bartel, *Biochemistry* **42**, 8748 (2003).
16. M. S. Lawrence, D. P. Bartel, *RNA* **11**, 1173 (2005).
17. M. P. Robertson, A. D. Ellington, *Nucleic Acids Res.* **28**, 1751 (2000).
18. M. P. Robertson, A. D. Ellington, *Nat. Biotechnol.* **19**, 650 (2001).
19. M. P. Robertson, S. M. Knudsen, A. D. Ellington, *RNA* **10**, 114 (2004).
20. M. P. Robertson, J. R. Hesselberth, A. D. Ellington, *RNA* **7**, 513 (2001).
21. See RNA preparation in materials and methods, available as supporting material on *Science* Online.
22. See crystallization and structural solution in materials and methods, available as supporting material on *Science* Online.
23. H. W. Pley, K. M. Flaherty, D. B. McKay, *Nature* **372**, 68 (1994).
24. W. G. Scott, J. T. Finch, A. Klug, *Cell* **81**, 991 (1995).
25. M. Martick, W. G. Scott, *Cell* **126**, 309 (2006).
26. D. Bandyopadhyay, D. Bhattacharyya, *J. Biomol. Struct. Dyn.* **21**, 447 (2003).

27. We thank A. Ellington, H. Noller, members of the Scott laboratory and of the RNA Center at UCSC for helpful discussions and support, and the NIH and W. M. Keck Foundation for funding. We dedicate this paper to Professor Stanley L. Miller. Coordinates and data: F_{obs} and coordinates have been deposited with Protein Data Bank accession code 2OIU. These data, as well as the composite-omit $2F_{obs} - F_{calc}$ and other electron density maps described in the paper, are available from http://xanana.ucsc.edu/L1.

Supporting Online Material

www.sciencemag.org/cgi/content/full/315/5818/1549/DC1
Materials and Methods
Figs. S1 and S2
Table S1
References

12 October 2006; accepted 25 January 2007
10.1126/science.1136231

Resonant Amplification of Magnetic Domain-Wall Motion by a Train of Current Pulses

Luc Thomas,* Masamitsu Hayashi, Xin Jiang, Rai Moriya, Charles Rettner, Stuart Parkin*

The current-induced motion of magnetic domain walls confined to nanostructures is of interest for applications in magnetoelectronic devices in which the domain wall serves as the logic gate or memory element. The injection of spin-polarized current below a threshold value through a domain wall confined to a pinning potential results in its precessional motion within the potential well. We show that by using a short train of current pulses, whose length and spacing are tuned to this precession frequency, the domain wall's oscillations can be resonantly amplified. This makes possible the motion of domain walls with much reduced currents, more than five times smaller than in the absence of resonant amplification.

Recent theoretical (*1*–*5*) and experimental (*6*–*14*) work has focused on the manipulation of magnetic domain walls (DWs) in nanoscaled magnetoelectronic devices by means of spin-polarized current passing directly through the DW. Current-induced motion of DWs has distinctly different characteristics from their motion brought about by magnetic fields, making it particularly useful for memory storage applications (*15*). For metallic nanowires (typically permalloy, $Ni_{81}Fe_{19}$), current-driven DW motion occurs only at zero or low magnetic fields if the current density exceeds a threshold value on the order of 10^8 A/cm^2. It is not yet clear whether this threshold has a fundamental origin or is related to pinning sites in the nanowires. Nevertheless, such high current densities are impractical for device applications, and it is crucial to find ways to reduce this threshold value.

Spin-polarized current injected across a DW confined to a pinning potential results in damped oscillations of the DW within the potential well, in which the DW position along the nanowire oscillates out of phase with its momentum (*14*). Here we show that oscillations in the DW position and momentum can be resonantly

IBM Almaden Research Center, 650 Harry Road, San Jose, CA 95120, USA.

*To whom correspondence should be addressed. E-mail: lucthom@us.ibm.com (L.T.); parkin@almaden.ibm.com (S.P.)

amplified by using a short sequence of current pulses, whose lengths and separations are tuned to its oscillation frequency.

We first introduce a one-dimensional (1D) analytical model to describe the resonant depinning of a DW from a parabolic potential well. Such a well mimics an intrinsic or artificially created defect, such as a notch, in the nanowire. The 1D model was first introduced to describe the field-induced dynamics of DWs (*16*) and has recently been extended to include interactions with spin-polarized current (*1*–*5*). In this model, the DW dynamics can be described by just two variables: the DW position q and the angle Ψ by which the DW's magnetization is tilted out of the plane of the nanowire. The deviation of Ψ from its equilibrium value is akin to the DW's momentum (*17*).

The temporal evolution of q and Ψ for a DW excited by dc current and by single and several current pulses, each of the same amplitude as the dc current, are compared in Fig. 1A. The current density is expressed in terms of the spin torque amplitude, which has the dimension of a velocity. For dc current (Fig. 1A, a panels), both q and Ψ oscillate, out of phase with each other, but with the same characteristic frequency. The latter is related to the DW's mass and the slope of the pinning potential (*13*, *14*). The oscillation amplitude decreases with time because of Gilbert damping. Figure 1A (b panels) shows clearly that using short current pulses as compared to the damping time can lead to amplification of the DW's oscillations. Amplification occurs when the current is cut off at times close to odd multiples of half the precession period when q is close to zero (the DW is near the center of the well) and Ψ is large. When the DW is only weakly pinned, the amplification of the DW's motion induced by a single current pulse may be sufficient to depin the DW (*14*). However, for stronger pinning potentials, additional properly timed current pulses can further amplify the DW's motion within the well. This occurs, for example, when two half-period long pulses of the same current polarity are injected into the DW separated by a half-period spacing (Fig. 1A, c panels). Amplification is even larger when successive current pulses of opposite polarities are used (Fig. 1A, d panels).

The mechanism responsible for the resonant amplification of the DW's trajectory can be understood by considering its trajectory in position/momentum phase space (Fig. 1B). In the absence of current, the DW is at $q = 0$, $\Psi = 0$ (black dot in Fig. 1B). With sufficiently long pulses, the DW spirals toward a new equilibrium state at $q = 0$ and a nonzero value of Ψ (negative for positive current), as shown by the red dot in Fig. 1B (see also a panels in Fig. 1A). At any given point in time, the DW's trajectory is a spiral toward an equilibrium point along the $q = 0$ axis but with different Ψ values, depending on the current amplitude and polarity. For example, when the current is suddenly turned off, the DW circles toward the point $q = 0$, $\Psi = 0$. If this happens when the DW has high momentum (large $|\Psi|$), then the initial radius of its new trajectory is increased so that the DW undergoes a larger excursion than it would otherwise have done with a longer current pulse. An even larger increase in the amplitude of the DW's orbit results if the current direction is

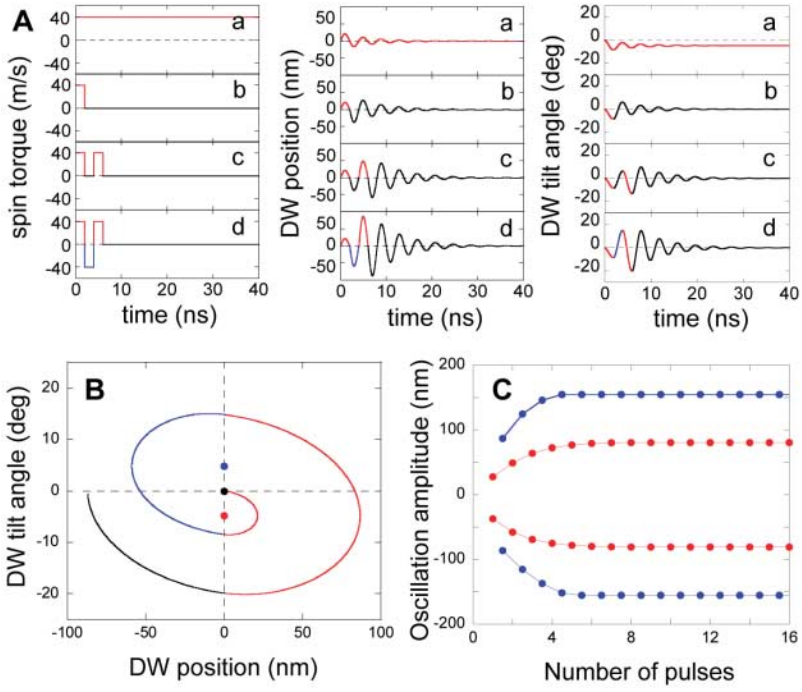

Fig. 1. (**A**) Pulse patterns, DW position, and DW tilt angle as a function of time, calculated using the 1D model (*17*). The deviation of the DW's tilt angle from its equilibrium value is proportional to the DW's momentum. (**B**) Trajectory of the DW in position/momentum phase space for 1.5 bipolar pulses. Dots show the equilibrium positions for zero (black), positive (red), and negative (blue) current. (**C**) Maximal values of the DW displacement along positive and negative directions for unipolar (red) and bipolar (blue) patterns of pulses at resonance.

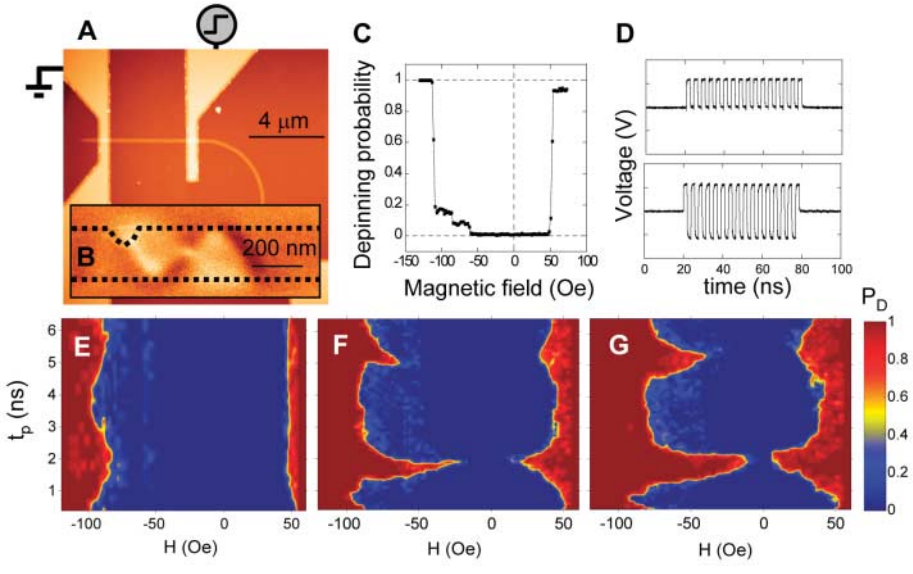

Fig. 2. (**A**) Atomic force microscopy (AFM) image of the permalloy nanowire and its electrical contacts. (**B**) Magnetic force microscopy image of a vortex DW pinned at the notch. Dashed lines show the edges of the wires as determined from the corresponding AFM image. (**C**) Probability of depinning a DW from the notch versus applied magnetic field. (**D**) Examples of pulse patterns: 16 unipolar pulses (top panel) and 15.5 bipolar pulses (bottom panel). (**E** to **G**) DW P_D at a constant pulse voltage of 1 V versus magnetic field H and pulse length t_p, for a single pulse (E), 16 unipolar pulses (F), and 15.5 bipolar pulses (G).

reversed rather than switched off, because the new equilibrium point is further away at a positive value of Ψ (blue dot in Fig. 1B). The amplitude of the DW's circling trajectory can be further increased by using a succession of properly timed unipolar or bipolar current pulses. However, because of Gilbert damping, this effect saturates after a few pulses, for reasonable values of the damping constant α (for example, α = 0.01 in Fig. 1C). If the resonantly amplified DW motion exceeds the extent of the pinning potential, it follows that the DW will be depinned. The depinning current can thereby be reduced by an order of magnitude (*17*).

The predictions of the model were tested in a 200-nm-wide, 40-nm-thick permalloy nanowire (Fig. 2A). Experimental details can be found in (*14*, *17*). A triangular notch 120 nm wide and 70 nm deep, fabricated on one side of the wire, acted as a pinning site for the DW. A DW was positioned at the notch and was detected by its dc resistance. Magnetic force microscopy showed that the DW had a vortex structure (Fig. 2B). The strength of the pinning potential can be estimated from the fields required to depin the DW in the absence of current. Positive and negative fields drive the DW away from and across the notch, respectively. DWs were depinnned with a probability higher than 0.5 when the field magnitude H exceeded $H_D^+ = +53$ Oe and $H_D^- = -111$ Oe (D, depinning), respectively, for positive (+) and negative (–) fields (Fig. 2C). The current-induced depinning of the DW from the notch was probed by applying a series of current pulses between two contacts to the nanowire (Fig. 2A). A static magnetic field was also used to assist DW motion in either direction along the nanowire. The device resistance was measured before and after the injection of the current pulses to probe whether the DW had been depinned. This sequence was repeated 10 times under each set of conditions to determine the probability of depinning the DW, P_D. Two types of current pulse patterns were used, hereafter referred to as unipolar or bipolar (Fig. 2D, top and bottom panels, respectively). Positive voltage corresponds to current flowing from right to left in Fig. 2A (*17*).

Maps of P_D are shown in Fig. 2, E to G, for a constant pulse amplitude V_p = 1.0 V (corresponding to ~10^8 A/cm^2) as a function of the pulse length t_p and magnetic field H applied during the pulse. When a single pulse was applied (Fig. 2E), the DW only depinned when aided by large magnetic fields, and $H_D^+ \sim 48$ Oe was essentially independent of the pulse length t_p. In contrast, H_D^- exhibited slight oscillations between –84 Oe and –98 Oe as a function of t_p. This behavior can be explained by the precessional motion of the DW excited by current (*14*). When the current pulse length matches an odd multiple of half the precession period, the DW is depinned in slightly smaller fields. However, because the pinning from the notch is quite strong, this effect is observed only when the field is close to the zero-current depinning field. A much larger effect was observed for a train of 16 unipolar (Fig. 2F) or bipolar (Fig. 2G) pulses. In these cases, the depinning fields became extremely sensitive to the pulse length. Both H_D^+ and H_D^- were strongly reduced for $t_p \sim 1.9$ ns and also, to a lesser extent, for $t_p \sim 5.7$ ns (*18*).

Figure 3, A to C, shows maps of P_D for series of 16 pulses of a fixed length of 1.9 ns, corresponding to the first resonance peak of Fig. 2, F and G, as a function of the pulse amplitude and magnetic field. In the first case (Fig. 3A), there was no spacing between the pulses (the sequence was a single pulse of length 30.4 ns), and the critical current increased rapidly when the field was reduced. The data are asymmetric for positive and negative fields because of the asymmetry of the pinning potential profile (*12*). By contrast, the polarity of the current plays very little role in this regime of field-assisted current-driven depinning. For a sequence of 16 unipolar pulses (Fig. 3B), the critical current was strongly reduced. The depinning fields were reduced to ~ ±15 Oe for 1.0-V pulses. These depinning fields were essentially unchanged for higher pulse amplitudes, although they increased slightly at the highest amplitudes. For a sequence of 16 bipolar pulses (Fig. 3C), the critical current reduction was even more pronounced. Depinning fields were reduced to ±10 Oe for 0.5-V pulses. This represents a reduction of the critical current by a factor of more than 5 as compared to the single-pulse case. No zero-field depinning was observed, even for pulse amplitudes much larger than 0.5 V. We suggest that this is related to the tails of the pinning potential well from the notch, which may extend over long distances, most likely due to the elasticity of the DW profile, which is not included in the 1D model discussed above. Thus, in the absence of field, the DW probably remains trapped at the end of the sequence of current pulses, even though the DW may have moved a long distance. Such a behavior is well reproduced with the 1D model when, for example, a Lorentzian-shaped potential well is used. Tailoring the pinning potential profile by changing the notch shape and depth or by stiffening the magnetic material may allow for resonant DW depinning in zero field.

Finally, we explored the coherence time of the current-induced DW resonant motion by using a sequence of two unipolar or bipolar pulses. The pulse length was varied from 0.4 to 3.4 ns, corresponding to the first resonance peak in Fig. 2, F and G, and the interval between the center of the two pulses t_I was increased from 0 to 45 ns (i.e., $t_I = 0$ when the two pulses overlap one another). In this pump-probe experiment, the first pulse excites the precessional motion of the DW. Depending on the phase and amplitude of the DW precession at the time of the second probe pulse, the DW may or may not be depinned. Results are shown in Fig. 4 for a constant pulse amplitude V_p = 1.3 V and a constant field H = –69 Oe. Oscillations in P_D are clearly observed as a function of the time interval between the two pulses, which persist for times as long as

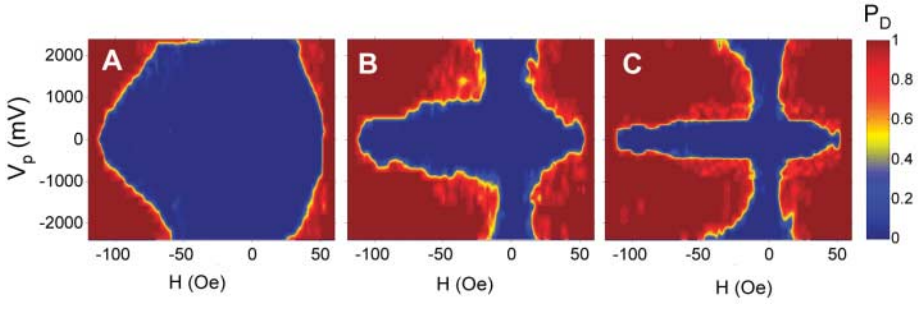

Fig. 3. DW P_D at constant pulse length versus magnetic field H and pulse amplitude V_p for different pulse patterns: (**A**) a single pulse 30.4 ns long; (**B**) 16 unipolar pulses, each 1.9 ns long (Fig. 2F); and (**C**) 15.5 bipolar pulses, each 1.9 ns long (Fig. 2G).

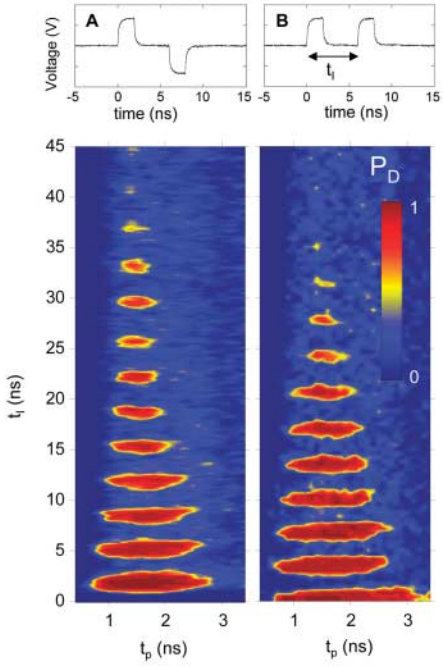

Fig. 4. DW P_D at constant magnetic field H = –69 Oe and pulse amplitude V_p = 1.3 V for a sequence of two pulses versus pulse length t_p and interval between the two pulses t_I for (**A**) bipolar pulses and (**B**) unipolar pulses. Pulse profiles are shown in the top two panels.

40 ns. As t_I is progressively increased, Gilbert damping causes the amplitude of the oscillations to decrease, so that depinning is observed only in an increasingly narrower range of t_I and t_p.

In good agreement with the 1D model, the probability of DW depinning on t_I occurs out of phase for unipolar and bipolar pulses. For unipolar pulses, the second pulse leads to DW depinning when the interval is a multiple of the precession period, whereas for bipolar pulses, depinning is observed for odd multiples of half the precession period.

By using the concept of resonant amplification, DWs can be excited and moved with much reduced power, and, moreover, by tailoring pinning potentials, individual DWs in neighboring sites can be addressed. These results thus facilitate magnetoelectronic memory and logic devices with functionalities that are not possible with charge-based devices.

References and Notes

1. Z. Li, S. Zhang, *Phys. Rev. B* **70**, 024417 (2004).
2. G. Tatara, H. Kohno, *Phys. Rev. Lett.* **92**, 086601 (2004).
3. S. E. Barnes, S. Maekawa, *Phys. Rev. Lett.* **95**, 107204 (2005).
4. S. Zhang, Z. Li, *Phys. Rev. Lett.* **93**, 127204 (2004).
5. A. Thiaville, Y. Nakatani, J. Miltat, Y. Suzuki, *Europhys. Lett.* **69**, 990 (2005).
6. N. Vernier, D. A. Allwood, D. Atkinson, M. D. Cooke, R. P. Cowburn, *Europhys. Lett.* **65**, 526 (2004).
7. A. Yamaguchi *et al.*, *Phys. Rev. Lett.* **92**, 077205 (2004).
8. M. Klaui *et al.*, *Phys. Rev. Lett.* **95**, 026601 (2005).
9. M. Klaui *et al.*, *Phys. Rev. Lett.* **94**, 106601 (2005).
10. M. Yamanouchi, D. Chiba, F. Matsukura, H. Ohno, *Nature* **428**, 539 (2004).
11. D. Ravelosona, D. Lacour, J. A. Katine, B. D. Terris, C. Chappert, *Phys. Rev. Lett.* **95**, 117203 (2005).
12. M. Hayashi *et al.*, *Phys. Rev. Lett.* **97**, 207205 (2006).
13. E. Saitoh, H. Miyajima, T. Yamaoka, G. Tatara, *Nature* **432**, 203 (2004).
14. L. Thomas *et al.*, *Nature* **443**, 197 (2006).
15. S. S. P. Parkin, U.S. Patent 6,834,005 (2004).
16. A. P. Malozemoff, J. C. Slonczewski, *Magnetic Domain Walls in Bubble Material* (Academic Press, New York, 1979).
17. More details are available as supporting material on *Science* Online.
18. The second resonance occurs for pulse lengths of 3/2 oscillation periods, which is three times longer than that of the first resonance (1/2 oscillation period).

19. We acknowledge financial support from Defense Microelectronics Activity.

Supporting Online Material

www.sciencemag.org/cgi/content/full/315/5818/1553/DC1
Materials and Methods
Fig. S1
Reference

16 November 2006; accepted 16 January 2007
10.1126/science.1137662

Critical Behavior of a Trapped Interacting Bose Gas

T. Donner,[1] S. Ritter,[1] T. Bourdel,[1] A. Öttl,[1] M. Köhl,[1,2]* T. Esslinger[1]

The phase transition of Bose-Einstein condensation was studied in the critical regime, where fluctuations extend far beyond the length scale of thermal de Broglie waves. We used matter-wave interference to measure the correlation length of these critical fluctuations as a function of temperature. Observations of the diverging behavior of the correlation length above the critical temperature enabled us to determine the critical exponent of the correlation length for a trapped, weakly interacting Bose gas to be $\nu = 0.67 \pm 0.13$. This measurement has direct implications for the understanding of second-order phase transitions.

Phase transitions are among the most striking phenomena in nature. At a phase transition, minute variations in the conditions controlling a system can trigger a fundamental change of its properties. For example, lowering the temperature below a critical value creates a finite magnetization of ferromagnetic materials or, similarly, allows for the generation of superfluid currents. Generally, a transition takes place between a disordered phase and a phase exhibiting off-diagonal long-range order, which is the magnetization or the superfluid density in the above cases. Near a second-order phase transition point, the fluctuations of the order parameter are so dominant that they completely govern the behavior of the system on all length scales (*1*). In fact, the large-scale fluctuations in the vicinity of a transition already indicate the onset of the phase on the other side of the transition.

Near a second-order phase transition, macroscopic quantities show a universal scaling behavior that is characterized by critical exponents (*1*) that depend only on general properties of the system, such as its dimensionality, symmetry of the order parameter, or range of interaction. Accordingly, phase transitions are classified in terms of universality classes. Bose-Einstein condensation in three dimensions, for example, is in the same universality class as a three-dimensional XY model for magnets. Moreover, the physics of quantum phase transitions occurring at zero temperature can often be mapped onto thermally driven phase transitions in higher spatial dimensions.

The phase transition scenario of Bose-Einstein condensation in a weakly interacting atomic gas is unique, as it is free of impurities and the two-body interactions are precisely known. As the gas condenses, trapped bosonic atoms of a macroscopic number accumulate in a single quantum state and can be described by the condensate wave function, the order parameter of the transition. However, it has proven to be experimentally difficult to access the physics of the phase transition itself. In particular, the critical regime has escaped observation because it requires an extremely close and controlled approach to the critical temperature. Meanwhile, advanced theoretical methods have increased our understanding of the critical regime in a gas of weakly interacting bosons (*2*–*5*). Yet a theoretical

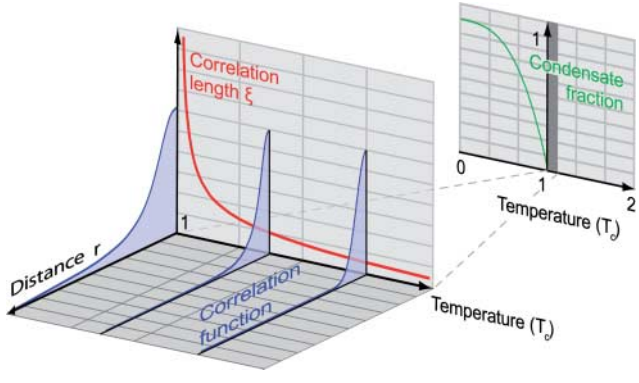

Fig. 1. Schematics of the correlation function and the correlation length close to the phase transition temperature of Bose-Einstein condensation. Above the critical temperature T_c the condensate fraction is zero, and for $T >> T_c$ the correlation function decays approximately as a Gaussian on a length scale set by the thermal de Broglie wavelength λ_{dB}. As the temperature approaches the critical temperature, long-range fluctuations start to govern the system and the correlation length ξ increases markedly. Exactly at the critical temperature, ξ diverges and the correlation function decays algebraically for $r > \lambda_{dB}$ (Eq. 1).

[1]Institute of Quantum Electronics, Eidgenössische Technische Hochschule (ETH) Zürich, CH-8093 Zürich, Switzerland. [2]Cavendish Laboratory, University of Cambridge, Cambridge CB3 0HE, UK.

*To whom correspondence should be addressed. E-mail: koehl@phys.ethz.ch